Stirring with the phase angle ϕ: Unlocking chaos in slow subperiodic viscous flows

Prabhash Kumar, Prahallada Jutur, Anubhab Roy, and Mahesh Panchagnula
Department of Applied Mechanics, Indian Institute of Technology Madras, Chennai 600036, India

(Received 13 March 2024; accepted 30 April 2025; published 3 June 2025)

We conduct experimental and numerical investigations to understand how subperiodic variability in oscillatory flows drives fluid stirring and facilitates the transition to chaos in slow viscous flows. Our work introduces pulsatile fluid flow through a bifurcating network called the T-section model, which incorporates piston assemblies driven by stepping motors. In this configuration, the velocity disparity between the pistons—defined by the phase angle ϕ—is the basis for subperiodic variability. The interplay between ϕ and the normalized oscillation frequency f governs the transition from regular to chaotic trajectories. Our analyses identify that this subperiodic variability within the bifurcating T-section setup results in the coexistence of open and closed streamlines, with periodic switching between them effectively driving stretch-and-fold mechanisms that are crucial for stirring. We have created a regime map in the f-ϕ parameter space to identify regions of chaotic and nonchaotic stirring while also delineating the boundaries of the chaotic zone. These findings highlight the significant role of subperiodic variability in enhancing stirring within viscous flows, with broad implications for transportation and mixing processes in physical, biological, and industrial systems.

DOI: 10.1103/PhysRevFluids.10.064101

I. INTRODUCTION

Mixing in slow viscous flows plays crucial roles across various environmental, physiological, and engineering applications. In oceanic environments, chaotic mixing is vital for distributing heat and oxygen to the seabed and evenly spreading nutrients and plankton throughout marine ecosystems [1,2]. Similarly, chaotic fluid trajectories enhance mixing in microfluidic devices [3], while mechanically induced chaotic mixing improves energy efficiency and mixing quality in industries such as food processing, pharmaceuticals, chemicals, and semiconductors [4–6].

In this study, we examine a bifurcating network with pulsatile boundary conditions, generating slow, viscous flow, to explore how velocity disparity in these boundary conditions can induce mixing without relying on particle diffusion or turbulent flow. Pulsatile flows in bifurcating networks are critical in physiological contexts, such as pulmonary and blood flows, and industrial applications like micromixers. In many practical settings, such as pulmonary airflow in the lung acinus, flow oscillations lack synchronization due to the geometry. The irregular shape of the acinar walls leads to asynchronous deformation, resulting in uncoordinated expansion and contraction. Our study is inspired to investigate the effects of nonuniform expansion and contraction observed in lung alveoli.

Airflow in the lung airways transitions from the nasal passage to the alveoli, where gas exchange occurs. The fluid dynamics vary significantly, with Reynolds numbers ranging from $O(10^3)$ in the trachea to $O(10^{-3})$ in the acinar region [7–11]. In the acinus, flow is primarily quasi-steady and viscous-dominated, which is vital for adequate gas exchange. Previous studies [12–14] characterized acinar flow as kinematically reversible; however, Tsuda and colleagues identified a saddle point near the alveolar openings, suggesting potential chaotic flow [15–18]. While particle inertia is negligible and impaction is minor, increased mixing in this region is crucial for understanding pulmonary

diseases. Recent research highlights that nonuniform movement of alveolar walls may significantly influence particle trajectories in deeper lung areas, where the airflow is calm (dominated by viscous forces), and diffusion-driven mixing is the primary mechanism at play [19–22]. Diffusion-driven mixing is less effective for particles with lower diffusion constants, as this process occurs at a slower time scale. Therefore, mixing enhanced by chaotic stretching becomes crucial [23].

The time-dependent, two-dimensional (2D) dynamical systems that adhere to fluid incompressibility can produce chaotic trajectories, as demonstrated by various experimental and numerical studies [24–28] following the foundational work of Aref [29]. These studies emphasize the significance of the wrapping action around the elliptic fixed point, referred to as a "whorl" and the stretching and compression near the hyperbolic fixed points, known as "tendrils" in generating patterns that are smaller than the flow scale [30]. Aref and Balachandar [31] examined the influence of time modulation on fluid trajectories, identifying that chaotic motion can arise even in the presence of strong viscous damping. Furthermore, Hackborn *et al.* [32] underscored the significance of the often-overlooked degenerate mixing zone, which is as crucial as the hyperbolic mixing zone. More recent studies have addressed how wall effects can diminish global mixing efficiency and have emphasized the role of rotating boundary conditions in establishing a transport barrier that separates the global mixing zone from its surroundings [33–35].

We employ experimental and numerical techniques to explore the stirring mechanisms within a slow, viscous oscillatory flow occurring through a bifurcating geometry. Our primary objective is to understand the influence of asymmetric oscillation and oscillation frequency on fluid stirring mechanism and their subsequent transition to chaos. This study examines explicitly the stirring mechanism in pulsatile flows through a T-junction configuration. Although the terms "stirring" and "mixing" are often used interchangeably, they refer to distinct physical processes. As articulated by Villermaux [36], mixing entails the agitation of scalar fields by flow coupled with molecular diffusion, ultimately resulting in homogenization. In the present work, we focus exclusively on the stirring aspect, analyzing how pulsatile flow fields stretch and fold material lines to create conditions that favour eventual mixing. Notably, this investigation deliberately omits the consideration of molecular diffusion. In Sec. II, we outline our experimental apparatus and the operating conditions. We then detail the numerical methods in Sec. III. In Sec. IV, we present both experimental and simulation results alongside a thorough discussion of the key findings of this study. Finally, we summarize the essential insights in Sec. V.

II. APPARATUS AND EXPERIMENTAL CONDITIONS

Our experimental setup consists of an inverted T-section model with two horizontal arms connected to a piston-motor assembly and a third, vertically oriented arm open to the atmosphere. The T-section has a uniform square cross-section of 20×20 mm, forming the core of our apparatus. We position it on the test table so that the vertical arm aligns upright when the horizontal arms rest on the table. The horizontal arms measure 8 cm in length and connect to independent piston-motor systems, while the vertical arm extends 12 cm. Each motor drives its piston with precise, time-periodic motion, crucial for simulating the oscillatory flows, like breathing. As shown in Fig. 1, this apparatus establishes a controlled environment for studying oscillatory viscous flows. By adjusting the pistons' motion and varying flow parameters, we systematically explore fluid mechanics within oscillatory processes, enabling us to model complex flow patterns and analyze their effects on transport behavior.

We utilize the infuse/withdraw programmable Harvard pump 11 Elite with 0.9° stepping and $1/16$ microstepping to drive the pistons in our experimental setup. These pumps deliver flow rates ranging from 43.680 nl/min to 45.360 ml/min when using a 20 ml syringe. We can program the pumps to operate with or without a computer. We connect the stepper motors as two units via USB ports and control them with ASCII commands written in Python. This setup allows us to rhythmically drive the pistons to infuse and withdraw fluid into the system, generating a slow, viscous flow. We prescribe a nominal piston velocity of $\mathbf{V}_0 = 1.25$ mm/s to achieve sufficiently low

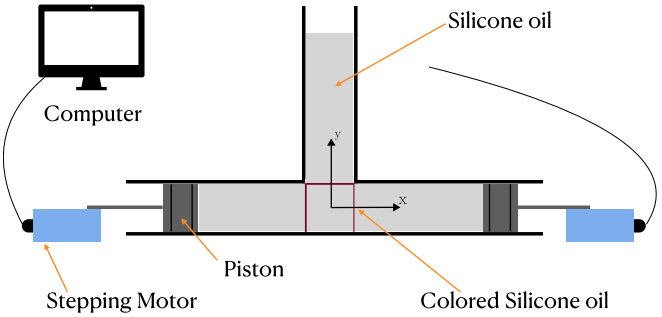

FIG. 1. Schematic of the experimental setup where the central component is a T-section. Different components of the setup are indicated in the figure.

Reynolds number, Re = 0.0025, with channel dimension of $L = 20$ mm and viscosity of working fluid 10 000 CSt ($\nu = 0.01$ m^2/s), where ν is the kinematic viscosity of the working fluid (silicone oil). The oscillation time scale, $O(1)$, is much greater than the viscous diffusion scale, $a^2/\nu = 0.04$; hence, the effects of temporal fluid inertia are negligible.

We introduce subperiodic variability using a parameter ϕ, representing the disparity in piston velocities, as described by Tsuda *et al.* [19]. The velocities of the right piston, $\mathbf{V}_R$, and the left piston, $\mathbf{V}_L$, are given by the following piecewise expression:

$$(\mathbf{V}_R, \mathbf{V}_L) = \begin{cases} (-\mathbf{V}_0, -\mathbf{V}_1), & 0 \leqslant t < \frac{T}{4}, \\ (\mathbf{V}_1, \mathbf{V}_0), & \frac{T}{4} \leqslant t < \frac{2T}{4}, \\ (\mathbf{V}_0, \mathbf{V}_1), & \frac{2T}{4} \leqslant t < \frac{3T}{4}, \\ (-\mathbf{V}_1, -\mathbf{V}_0), & \frac{3T}{4} \leqslant t < T. \end{cases} \tag{1}$$

Here, $\mathbf{V}_0$ is the nominal velocity, and $\mathbf{V}_1 = \mathbf{V}_0(\sec\phi - \tan\phi)$ is the adjusted velocity based on ϕ. Additionally, $\mathfrak{f}^* = 1/T$ is defined as the dimensional oscillation frequency. Notice that the input piston velocity is in the form of square wave where velocity remains constant during a stroke while their direction can change during each subperiod. If $\phi = 0^\circ$, then both pistons move at the same velocity; if $\phi = 90^\circ$, then one piston is stationary. At $\phi = 180^\circ$, the pistons operate in opposite directions but at equal magnitudes, infusing or withdrawing fluid. The oscillatory piston motion is categorized as follows: (a) Symmetry ($\phi = 0^\circ$): Both pistons move together with $\mathbf{V}_1 = \mathbf{V}_0$. (b) Subperiodic variable ($0^\circ < \phi < 90^\circ$): One piston is always slower than the other, and pistons alternate their velocities in each quadrant. (c) Partially subperiodic variable ($90^\circ < \phi < 180^\circ$): One piston withdraws while the other infuses, causing less stretching to the fluid mass. (d) Reversed symmetry ($\phi = 180^\circ$): One piston always infuses while the other withdraws, minimizing fluid mass stretching. As ϕ approaches 90°, subperiodic variability peaks, while moving closer to 0° or 180° results in more symmetric behavior. An animation demonstrating the pistons' motion across these scenarios is available in the Supplemental Material [37] (Video 1).

We color the working fluid with oil-soluble Haksons Resin fluorescent pigment powder, ensuring that the physical properties of dyed oil remain unchanged, and manually inject the solution through the open vertical arm at the T-junction. We carefully draw the colored pattern (line element) much below the free surface to minimize the impact of surface effects on flow kinematics. While injecting the dye, we carefully place it in midplane of 3D square geometry to keep it away from the side wall. To enhance visibility, we illuminate the test area (the T-junction area) with an identical pair of Microspect UV lamps, each emitting light at a wavelength of 395 nm. We then capture high-resolution images using a Canon Tamron SP Di camera, which allows us to conduct detailed visualization and analysis of the deformation in line element observed in the experiments.

Despite the advanced capabilities of our apparatus, it does not precisely replicate the real lung acinus. While we capture critical aspects of alveolar flow kinematics, we simplify several complex features of the actual biological system. The uniform cross-section of the T-section and the idealized piston motion do not fully account for the irregular and highly variable geometry of real alveoli. Additionally, we conduct our model under controlled laboratory conditions that do not ideally mimic the physiological environment of the lungs, including factors such as tissue elasticity and variable airflow resistance in different lung regions. Nonetheless, our setup offers a powerful tool for studying the complex fluid kinematics and transport mechanisms in viscous oscillatory flows through a bifurcating geometry and *could be* essential in understanding the onset of chaos leading to efficient stirring in lung acinus. By varying the pistons' motion and adjusting the flow parameters, we systematically explore the key factors influencing the stirring processes within the lung acinus. This investigation offers valuable insights into the respiratory process that can inform medical research and applications, ultimately contributing to an improved understanding and treatment of respiratory conditions.

III. DETAILS ON NUMERICAL SIMULATIONS

We utilize COMSOL Multiphysics to conduct simulations that analyze the viscous pulsating fluid kinematics within the T-section model. In the simulation, we use a two-dimensional representation of our experimental setup, featuring a T-section with a width of 20 mm. The vertical arm of the T-section measures 12 cm in length, while each horizontal arm extends 8 cm. We employ the physics-controlled finer mesh feature of COMSOL to ensure the accurate representation of the intricate details inherent in fluid flow phenomena. Utilizing the Creeping Flow module, we model the low-Reynolds number flow (Re $\simeq 0.0025$) in the system and set the fluid properties to correspond with those of the silicone oil used in our experiments. We prescribe a pulsating velocity profile as a boundary condition for the horizontal arms, allowing them to move according to the specified velocities described by (1). A zero-pressure boundary condition is applied to the vertical arm of the T-section, while the remaining walls are rigid and adhere to no-slip wall boundary conditions. By extracting Eulerian flow data at regular intervals from COMSOL, we perform cubic interpolation in space and linear interpolation in time to calculate the Lagrangian fluid trajectories using the following equation:

$$\frac{d\mathbf{x}}{dt} = \mathbf{u}(\mathbf{x}, t), \tag{2}$$

where $\mathbf{x}$ represents the Lagrangian fluid position and $\mathbf{u}(\mathbf{x}, t)$ is the interpolated flow field function within the T-section domain. Notice that we use three-dimensional geometry in the experiments wherein the velocity field exhibits a variation along the depth direction. Specifically, the highest velocity occurs at the midplane, while the front and back walls exhibit zero velocity due to the no-slip boundary condition. In contrast, the two-dimensional simulations do not account for this variation and only represent the kinematics at the midplane. Let us denote the midplane centerline velocity in the experimental setup as U_c. This velocity relates to the average piston velocity, $\bar{U}_{\text{exp}}$, according to the relationship [38,39]

$$\frac{U_c}{\bar{U}_{\text{exp}}} = \frac{3}{2}\left(\frac{1 + 4\Sigma_{k=1}^{\infty}\frac{(-1)^k \operatorname{sech}\alpha_k}{\alpha_k^3}}{1 - 6\Sigma_{k=1}^{\infty}\frac{\tanh\alpha_k}{\alpha_k^5}}\right), \tag{3}$$

where $\alpha_k = (2\,k - 1)\pi/2$. For a two-dimensional channel flow scenario, the centerline velocity equals $3/2$ of the average velocity. It becomes necessary to adjust the average piston velocity in the simulation to reconcile the velocity profile in the two-dimensional simulation with that observed at

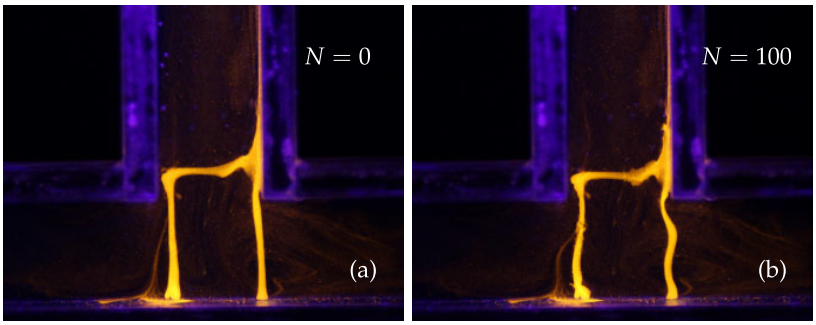

FIG. 2. Experimental visuals at (a) $N = 0$ and (b) $N = 100$ for $\phi = 0^\circ$, N is number of oscillation cycle.

the midplane in the experimental framework. Thus, we find that

$$\bar{U}_{\text{sim}} = \left(\frac{1 + 4\Sigma_{k=1}^{\infty} \frac{(-1)^k \text{sech}\alpha_k}{\alpha_k^3}}{1 - 6\Sigma_{k=1}^{\infty} \frac{\tanh \alpha_k}{\alpha_k^5}} \right) \bar{U}_{\text{exp}} \approx 1.39\, \bar{U}_{\text{exp}}, \tag{4}$$

where $\bar{U}_{\text{sim}}$ is the average velocity in two-dimensional simulation. This adjustment must be incorporated into the boundary conditions within the two-dimensional simulation to ensure that the simulation results align satisfactorily with the experimental data. By implementing this modification, the motion of the pistons can be accurately governed by the specified velocities as delineated in equation (1), augmented with the correction factor of 1.39.

IV. RESULTS AND DISCUSSION

The current study focuses on two key parameters: the subperiodic variable parameter ϕ and the normalized oscillation frequency, ƒ. We normalize the frequency using the inverse flow time-scale V_0/L, where $L = 20$ mm (the channel dimension), and V_0 is the nominal piston speed, both of which remain constant. We vary ϕ from 0° to 180° and adjust ƒ from 0.25 to 1 to explore the transition to chaotic stirring. We aim to observe how these variables influence fluid trajectories, explicitly investigating whether they lead to orderly or chaotic stirring patterns. During the experiments, we capture high-resolution images at intervals of one oscillation cycle, which we call phase-locked images. Additionally, we record real-time video to analyze dye deformation in various scenarios. In this study, we denote the number of oscillation cycles as N.

A. Experimental observations

Consider a scenario of a oscillation with $\phi = 0^\circ$, in which the pistons move with equal velocities. The inverted U-shaped material line introduced at the T-junction displays a regular and repeatable pattern. During each oscillation, the dye pattern stretches and compresses equally in both arms without significant folding, consistently returning to its initial configuration at the end of each cycle. This repeated restoration to the original state exemplifies well-ordered, periodic motion that does not result in stirring. The phase-locked images remain nearly identical even after 100 cycles; we do not observe any significant deformation in the line element, as shown in Fig. 2. This observation illustrates that fluid parcels follow the same paths without any stirring. The phenomenon, characterized by unchanged phase-locked images, indicates that the trajectories are time-periodic, suggesting that particles move along predictable, cyclic paths without disruption or blending. Notably, this nonstirring and time-periodic behavior is consistent across all values of ƒ, as long as ϕ remains fixed at either 0° or 180°. We have included supplemental experimental video (Video 2) that presents a series of phase-locked images to illustrate this no stirring case. This video corresponds to the case where $\phi = 0^\circ$ and ƒ $= 0.5$ [37].

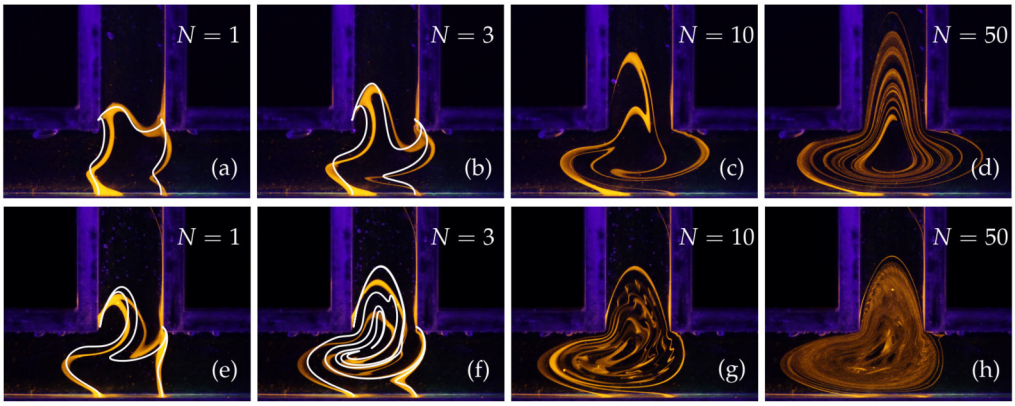

FIG. 3. The Poincaré maps of experimental images at $N = 1,\ 3,\ 10,$ and 50. Panels (a)–(d) correspond to the case of $\phi = 10^\circ$ at $\mathfrak{f} = 0.5$ and panels (e)–(h) correspond to $\phi = 90^\circ$ at $\mathfrak{f} = 0.5$. The white color pattern in panels (a), (b), (e), and (f) represent results from numerical simulation of the corresponding case.

However, an increase in ϕ beyond 0° leads to a significant shift in the system's behavior. The line element begins to deform, disrupting the formerly periodic time behavior, even though the piston motion exhibits a time-periodic motion. Under our experimental conditions, the line element shows finite deformation when $\phi \geqslant 5^\circ$ before it starts to diffuse. These deviations become more pronounced, and the fluid exhibits significant aperiodic deformations on increasing the ϕ. Figure 3 illustrates phase-locked images that demonstrate the deformation of line elements at $\phi = 10^\circ$ and $\phi = 70^\circ$ with $\mathfrak{f} = 0.5$. These images identify two distinct behavioral regimes based on the value of ϕ, highlighting how varying ϕ affect the deformation and stirring of the line elements over successive oscillation cycles (N). As shown in Figs. 3(a)–3(d), the stretch-fold mechanism at $\phi = 10^\circ$ leads to a regular and ordered structure. Even after first oscillation ($N = 1$) the dye pattern differs significantly from the initial pattern at $N = 0$, as shown in Fig. 3(a). As the oscillations continue, regular folding begins to occur, as illustrated in the Fig. 3(b) at $N = 3$, where the line element folds in a structured manner with minimal irregularity. By $N = 10$, the line element has developed well-defined, periodic layers, indicating that the oscillatory motion produces a regular, laminar and slow stirring of the dye, as shown in Fig. 3(c). The final stirred state at $N = 50$ resembles a stratified structure with distinct layers of dye separated by narrow gaps, as shown in Fig. 3(d). This organized laminar configuration indicates that at lower nonzero values of ϕ, the system maintains regularity with fluid stretching and folding that lead to fluid stirring. The layered structure resembles classic laminar flow, where different fluid layers slide past each other with minimal interaction, thus preserving the separation between dyed and undyed regions. The Supplemental Material, specifically Videos 3 and 4 [37], elucidate the deformation of the line element under continuous and phase-locked configurations, respectively, for the parameters set at $\phi = 10^\circ$ and $\mathfrak{f} = 0.5$ [37].

At a higher level of subperiodic variable, specifically $\phi = 90^\circ$, the sequencial stretch-fold mechanism, illustrated in Figs. 3(e)–3(h), results in a significantly different and much more chaotic state. The stirred state at $N = 1$ is more pronounced than $\phi = 10^\circ$ case as shown in Fig. 3(e). By the third cycle ($N = 3$), the pattern has already begun to deviate considerably from the smooth, orderly layered structure (see Fig. 3(f)) seen at $\phi = 10^\circ$. At this point, the layers overlap, twisting and deforming. As shown in Fig. 3(g), the stirred structure intensifies by $N = 10$ as the dye layers become increasingly entangled, showing a lack of the structured regularity that was present at lower ϕ values. As shown in Fig. 3(h), the stirred structure at $N = 50$ attains a completely homogeneous state, with no clear boundaries or separation between layers. This chaotic intermingling suggests that the oscillations introduce significant disturbances at higher ϕ, leading to complex and irregular

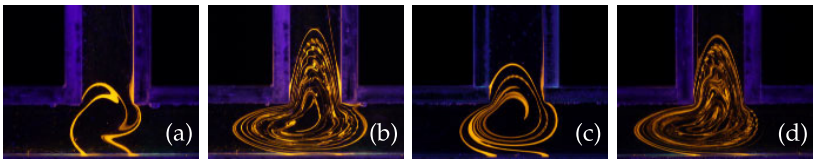

FIG. 4. Deformation of the material line (experimental visuals) at different angles $\phi = 50^\circ$ and $\phi = 70^\circ$ with varying $\mathfrak{f}$: (a) for $\phi = 50^\circ$, $\mathfrak{f} = 2$; (b) for $\phi = 50^\circ$, $\mathfrak{f} = 0.5$; (c) for $\phi = 70^\circ$, $\mathfrak{f} = 1$; and (d) for $\phi = 70^\circ$, $\mathfrak{f} = 0.5$. Images captured at $N = 20$.

deformations that enhance stirring throughout the observation field. The line element no longer maintains a stable structure; instead, it reflects a transition to a chaotic state. The continuous disruption of flow accelerates the breakdown of order, promoting stirring across the entire region. The Supplemental Material, particularly Videos 5 and 6 [37], provide a detailed elucidation of the emergence of fine-scale patterns smaller than the flow length scale, resulting in chaotic stirring phenomena under both continuous and phase-locked configurations. These observations were derived from experimental parameters set at $\phi = 90^\circ$ and $\mathfrak{f} = 0.5$ [37].

These experimental observations highlight the importance of ϕ as a critical factor in controlling the fluid stiring in oscillatory flows. When ϕ remains below a certain threshold, the system sustains a regular, laminar state that minimizes stirring, which can be advantageous for applications requiring structured flow patterns. However, as ϕ exceeds this threshold, the flow shifts to a chaotic state, enhancing stirring efficiency—a valuable characteristic for processes that demand rapid and thorough stirring. This transition from regular to chaotic stiring as ϕ increases underscores the sensitivity of fluid flows to subperiodic variability and provides insights into managing stirring processes across various applications.

We observed that when fluid motion loses periodicity at a nonzero (ϕ), a further decreasing ($\mathfrak{f}$) enhances irregularities in line element deformation, leading to chaotic behavior. Figure 4 shows the experimental images captured at $N = 20$ to emphasize the impact of $\mathfrak{f}$ on the stirring. In Figs. 4(a) and 4(b), we compare the line element deformations for $\mathfrak{f} = 2$ and $\mathfrak{f} = 0.5$ at $\phi = 50^\circ$. The deformation at the lower $\mathfrak{f}$ value of 0.5 exhibits chaotic characteristics, presenting irregular and complex shapes. Conversely, the deformation at the higher $\mathfrak{f}$ value of 2 is more regular and ordered, indicating a nonchaotic nature.

Figures 4(c) and 4(d) illustrate the deformation of line elements at $\mathfrak{f} = 1$ and $\mathfrak{f} = 0.5$ for an increased angle of $\phi = 70^\circ$. Even at this elevated ϕ, the pattern remains nonchaotic at the higher $\mathfrak{f} = 1$. At the same time, certain features hint at possible chaos when $\mathfrak{f} = 1$; these indications are not sufficiently pronounced to result in full chaotic behavior. Our experimental results indicate that synchronized oscillation at $\phi = 0^\circ$ or $\phi = 180^\circ$ leads to time-periodic deformations in the line element, which reverse after each oscillation. Interestingly, even the bifurcating arms do not contribute to the overall deformation. A nonzero ϕ is essential for disrupting these periodic deformations. At a given $\mathfrak{f}$, ϕ values close to 0° or 180° result in regular deformations that promote slower stirring. Conversely, an optimal ϕ near 90° produces irregular deformations that enhance stirring.

The following section will quantitatively assess stirring by analyzing simulation data. This analysis provides a detailed measure of the stirring process and its dependence on $\mathfrak{f}$ and ϕ. By taking this quantitative approach, we can better understand the conditions that lead to chaotic stirring and effectively characterize the stirring process.

B. Flow topology in bifurcating network—Blinking Moffatt eddies

The T-section exhibits various flow topologies even under steady conditions depending on the boundary conditions applied at each inlet/outlet. To investigate these behaviors, we consider three distinct boundary condition scenarios: (i) both horizontal arms (*I* and *II*) infuse flow into the

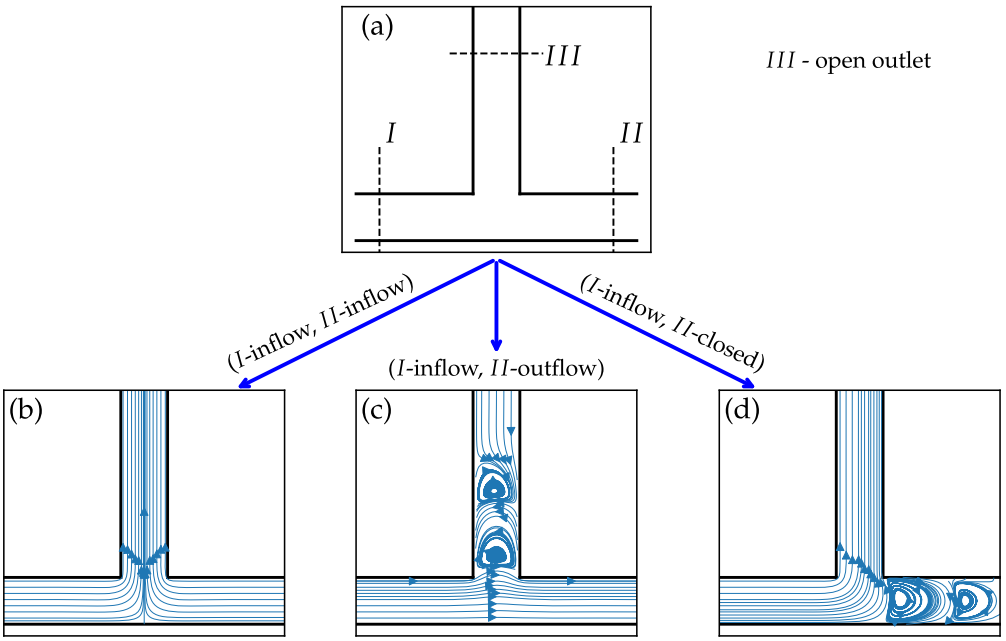

FIG. 5. Streamline patterns of Stokes flow in bifurcating network with different boundary conditions. (a) Schematic of simple bifurcating network T-section, (b) scenario (i) *I*—inflow boundary condition, *II*—inflow boundary condition, (c) scenario (ii) *I*—inflow boundary condition, *II*—outflow boundary condition, and (d) scenario (iii) *I*—inflow boundary condition, *II*—closed (impermeable) boundary condition. In this analysis, the boundary condition *III* is always an open outlet.

domain, (ii) the left arm infuses flow while the right arm withdraws, and (iii) the left arm infuses flow while the right arm remains closed. The vertical arm (*III*) is kept open in each scenario. In all of the scenarios, flow conditions are uniform with equal magnitude. In scenario (i), with arms I and II infusing flow at equal velocities, the two incoming streams converge at the T-junction and flow upwards into the third arm. Due to symmetry, a separatrix forms along the midline of the vertical arm with open streamlines on either side. This configuration, shown in Fig. 5(b), results in a stable, symmetric flow distribution along the T-section, with streamlines diverging smoothly into the vertical arm without recirculation. In scenario (ii), the left boundary infuses while the right boundary withdraws. This configuration produces a duct flow pattern, with an open region in the middle where the primary flow stream shears the fluid in the vertical channel. As a result, eddies emerge in the vertical arm, as shown in Fig. 5(c). This is akin to an array of Moffatt eddies [40] that form in lid-driven cavity flows of higher aspect ratio [41,42]. In scenario (iii), we set the left arm to infuse flow at a uniform velocity while the right arm remains closed (impermeable boundary). The streamlines turn into the third (vertical) arm, shearing the fluid in the right arm. This shearing action generates a series of Moffatt eddies in the right arm, as depicted in Fig. 5(d). These results demonstrate that even a simple bifurcating network like the T-section can yield diverse streamline topologies based on the inlet and outlet boundary conditions, producing open or closed streamline patterns.

C. Effects of time perturbation on streamlines

In this section, we analyze the effects of time modulation on the three scenarios considered in Sec. IV B. In scenario (i), switching the direction of the inflow boundary conditions does not change the streamline topology; it merely reverses the flow direction due to the symmetric boundary setup. Swapping the boundary conditions in scenario (ii) reverses the direction of the duct flow, and the

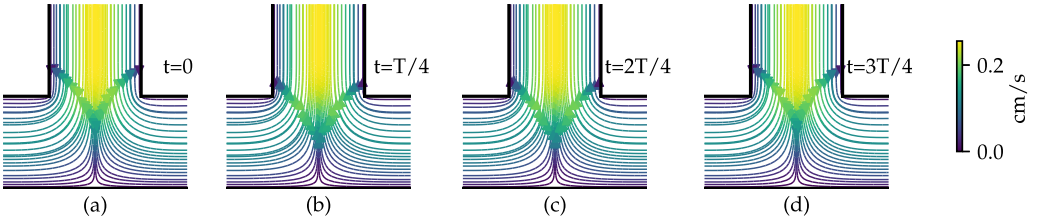

FIG. 6. Streamline patterns for $\phi = 0^\circ$ and $\mathfrak{f} = 0.5$ at (a) $t = 0$, (b) $t = T/4$, (c) $t = 2T/4$, and (d) $3T/4$.

eddies in the vertical arm rotate in the opposite sense. Scenario (iii) behaves differently: switching the boundary conditions significantly alters the flow kinematics. Each alteration replaces the closed streamlines with open ones, reversing the circulation within the eddies. The closed eddies in scenario (iii) exhibit whorl-like structures, while the open trajectories resemble tendrils, as described by Chaiken *et al.* [24] and Khakhar *et al.* [26]. In viscous flow, tendrils enhance fluid stretching, while whorls cause fluid folding. This periodic alternation between open and closed streamline patterns in scenario (iii) can produce chaotic fluid trajectories if the boundary conditions switch at the appropriate frequency. However, while open and closed streamline patterns are necessary conditions for chaotic stirring, they are not sufficient to guarantee it. As we will discuss further, these three flow scenarios reoccur within the system under varying ϕ.

First, we analyze the flow streamline patterns for $\phi = 0^\circ$ across different quadrants of an oscillation cycle. In the Figs. 6(a)–6(d), the phases $t = 0, t = T/4, t = 2T/4$, and $t = 3T/4$ correspond to distinct quadrants within a single oscillation cycle. When the piston velocities are equal, a flow separatrix forms along the midline of the vertical arm, remaining stationary throughout the oscillation cycle, as shown in Fig. 6. Although the flow direction changes in each quadrant based on the time-dependent inflow and outflow boundary conditions, the separatrix maintains its position, as a result streamlines from different phases do not overlap over each other. Consequently, we observe time-periodic fluid trajectories.

Due to the differences in velocity between the piston movements for $0^\circ < \phi < 180^\circ$, the flow separatrix shifts away from the midline of the vertical arm, aligning toward the low-flow stream. This shift occurs rapidly because of the step function nature of the input velocity.

Figures 7(a)–7(d) illustrate the streamline patterns for $\phi = 50^\circ$ and $\mathfrak{f} = 0.5$, highlighting the time-dependent behavior of fluid flow with a repetitive shift in the separation line (separatrix) corresponding to the changing piston velocities.

The streamline patterns in each quadrant demonstrate a notable shift in the separatrix away from the midline of the vertical arm, aligning toward the piston with a lower velocity. This shift in the separatrix occurs at twice the oscillation frequency. The half-cycle periodic movement of the separatrix is crucial, as it breaks the time-periodicity of fluid trajectories. As the separatrix shifts with each half-cycle, fluid particles on one side can cross over to the other side, leading to a phenomenon known as "streamline crossing" [27,28]. This feature is absent when $\phi = 0^\circ$ or $\phi = 180^\circ$. Consequently, fluid parcels do not follow repetitive paths,

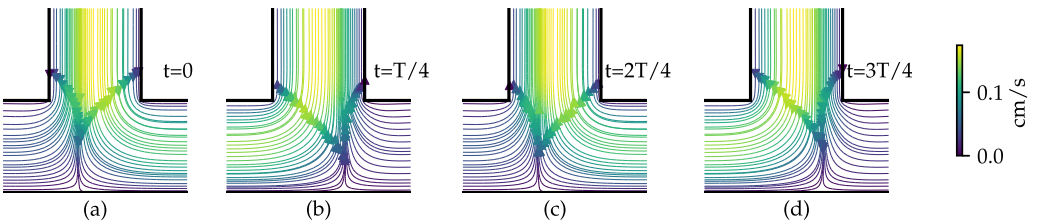

FIG. 7. Streamline patterns for $\phi = 50^\circ$ and $\mathfrak{f} = 0.5$ at (a) $t = 0$, (b) $t = T/4$, (c) $t = 2T/4$, and (d) $3T/4$.

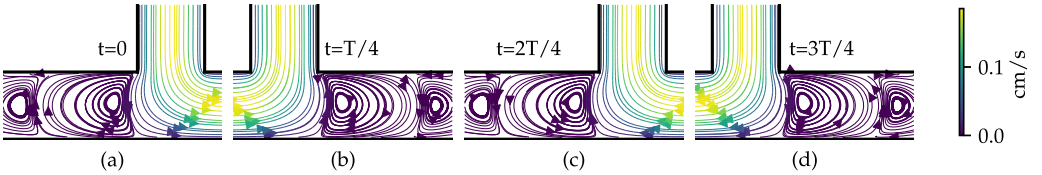

FIG. 8. Streamlines pattern (a) when left piston withdraws at a constant speed with right-side piston held stationary and (b) when right-side piston infuses at a constant speed with left-side piston held stationary. The color bar shows the velocity magnitude normalized with its maximum.

breaking the time-periodicity and resulting in the deformation of the line elements. This phenomenon exemplifies how asymmetry in the driving forces, such as the disparity in piston velocities, can fundamentally transform the flow structure, producing intricate, nonperiodic trajectories.

The time-modulated input velocities to the pistons differ fundamentally at $\phi = 90^\circ$ compared to other ϕ values. In this situation, only one piston moves at a time while the other remains stationary, preventing the formation of a separation line. However, this leads to an interesting flow feature. The flow bends toward the right when the right piston withdraws fluid in the first quadrant as shown in Fig. 8(a). This action shears the fluid layer in the left arm and creates closed eddy structures known as Moffatt eddies [40]. These structures trap fluid parcels in circulating paths, characterized by regions where streamlines loop back on themselves. Conversely, when the left piston infuses fluid in the second quadrant, a flow emerges that shears against the stationary fluid in the right arm, similarly generating Moffatt eddies and regions of closed streamlines on that side, as shown in Fig. 8(b). The similar flow structures emerge during the remaining two quadrants of oscillation, as shown in Figs. 8(c) and 8(d), indicating the emergence and periodic shift of these eddies with open streamlines.

The periodic transition between open and closed streamlines creates a stretch-and-fold action on fluid parcels, resulting in chaotic trajectories. It is important to note that even in steady flow conditions, open and closed streamlines can coexist. However, the trajectories remain nonchaotic when these streamlines do not switch positions. In this context, we highlight the significance of a bifurcating network in generating both open and closed streamlines and the importance of optimal time modulation to facilitate the transition of these streamlines to induce chaos.

Further analysis indicates that Moffatt eddies exist for various ϕ values other than 90°, although they remain hidden behind the predominant open streamlines. To visualize these eddies, we compute the residual velocity field $\mathbf{u}'(\mathbf{x}, t; \phi)$ by subtracting the velocity field at $\phi = 0^\circ$ from that at a nonzero ϕ:

$$\mathbf{u}'(\mathbf{x}, t; \phi) = \mathbf{u}(\mathbf{x}, t; \phi) - \mathbf{u}(\mathbf{x}, t; \phi = 0^\circ). \tag{5}$$

We illustrate $\mathbf{u}'(\mathbf{x}, t; \phi)$ for $\phi = 10^\circ$, $\phi = 70^\circ$, and $\phi = 90^\circ$ at $\mathfrak{f} = 0.5$ in Fig. 9. Introducing a velocity differential between the two pistons leads to the formation of Moffatt eddies due to the interactions between low and high flow streams, peaking at $\phi = 90^\circ$. In our case, the coexistence and periodic switching of open and closed streamlines contribute to stirring. However, the strength of the eddies (which depends on ϕ) and the residence time of fluid parcels within these eddies (which depends on $\mathfrak{f}$) determine the transition to chaotic stirring. Combining an optimal ϕ and lower $\mathfrak{f}$ shows that stirring can be chaotic; otherwise, the stirring is slow and nonchaotic.

D. Irreversible stirring

We performed a numerical simulation to investigate the stirring behavior when reversing the flow direction. We emphasized the differences between nonchaotic and chaotic stirring regimes, which depend on the parameters ϕ and $\mathfrak{f}$. We selected two sets of parameters that correspond to these distinct stirring regimes.

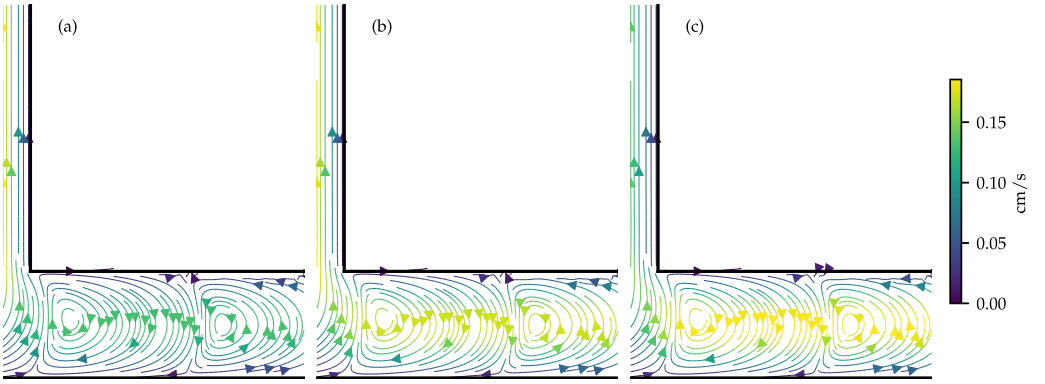

FIG. 9. Residual velocity field $\mathbf{u}'(\mathbf{x}, t; \phi)$ at $\mathfrak{f} = 0.5$ corresponding to (a) $\phi = 10°$, (b) $\phi = 70°$, and (c) $\phi = 90°$.

We started the investigation with two distinct initial patterns: a rectangle and a triangle. We tracked the positions of fluid particles over 30 cycles. After this, we reversed the flow direction and continued for another 30 cycles in the backwards direction. We used the final deformed patterns from the forward simulation as the initial conditions for the reversed simulation.

For the simulation, we select parameters ($\phi = 10°$, $\mathfrak{f} = 1$) for the nonchaotic case and ($\phi = 90°$, $\mathfrak{f} = 1/3$) for the chaotic case. In Fig. 10, we show the initial and deformed patterns corresponding to both cases. We observe that the deformation and stirring during the forward flow direction are more pronounced in chaotic cases than in nonchaotic ones. Furthermore, we can undo the deformation in the nonchaotic case by reversing the flow direction, but this is not possible in the chaotic stirring scenario. Additionally, the final mixed state in the chaotic case remains almost identical when we reverse the flow direction, regardless of the initial patterns.

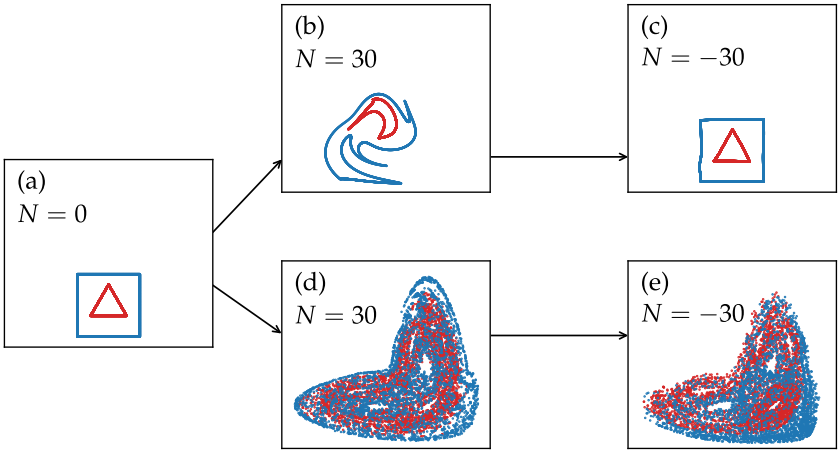

FIG. 10. The forward and reverse mapping of tracers over 30 cycles illustrates the distinction between nonchaotic and chaotic advection. Panel (a) shows the initial positions of fluid parcels arranged in two different configurations: a rectangle and a triangle. Panels (b) and (c) illustrate the forward and backwards maps of nonchaotic advection, respectively. In contrast, panels (d) and (e) depict the forward and backwards maps of tracer advection in the chaotic case. The initial conditions for the backwards simulation are the final positions from the forward simulation, with identical starting positions for both cases at $N = 0$.

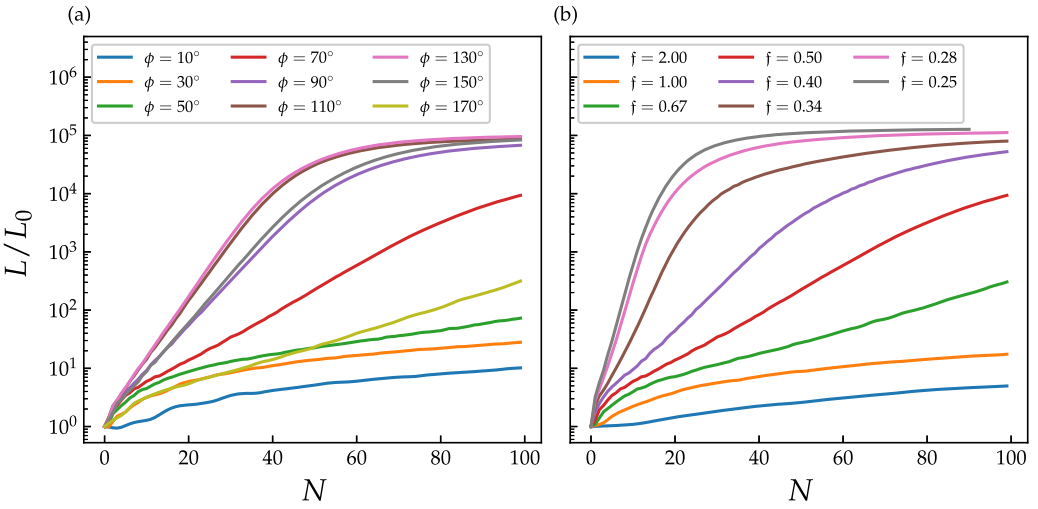

FIG. 11. (a) Evolution of line length for different ϕ at ʃ = 0.5 as a function of N, (b) evolution of line length for different ʃ at $\phi = 70°$ as a function of N. N represents the oscillation cycle number.

E. Line length growth

We measure the line length of deformed patterns using numerical simulation data, as directly measuring growth rates from experimental images is challenging due to the complex overlap and continuity of the line element deformations. To address this issue, we initialize thousands of particles in an inverted U-shaped pattern at the T-junction, similar to the initial configuration used in experiments at time $N = 0$. We then track the future positions of these particles by solving the governing equations of fluid motion [Eq. (2)] and utilizing the flow field computed from the numerical calculations. In Figs. 3(a) and 3(b) and Figs. 3(e) and 3(f), we compare the phase-locked stirred state obtained from our numerical simulations with the experimental results for the nonchaotic case ($\phi = 10°$, ʃ = 0.5) and the chaotic case ($\phi = 90°$, ʃ = 0.5), respectively. As illustrated in Figs. 3(a), 3(b), 3(e)), and 3(f), our numerical simulations effectively capture the stirring features observed in the experiments.

To evaluate how the line element evolves over time, which serves as a measure of stirring, we calculate the interparticle distances and determine the total length of the particle line using the following formula:

$$L(t) = \sum_{i=0}^{i=n} ||\mathbf{x}_{i+1}(t) - \mathbf{x}_i(t)||. \tag{6}$$

In this formula, n represents the number of particles, while $||\cdot||$ denotes the L_2 norm, which measures the Euclidean distance between the positions of the particles. As time progresses, the growth rate of the distances between particles, denoted by $L(t)$, indicates the degree of stirring.

We investigate how line lengths change in relation to N under two different scenarios to isolate the effects of ϕ and ʃ: (i) by keeping ʃ constant at 0.5 while varying ϕ, and (ii) by maintaining ϕ at 70° while varying ʃ. In both scenarios, the line elements increase with N and eventually plateau at a maximum length determined by the confinement. However, the time taken to reach this plateau varies depending on the parameters.

In the first scenario, the line length grows exponentially for the intermediate ϕ values, as shown in Fig. 11(a). The line length growth corresponding to $\phi = 130°$ is the fastest while the growth is slowest corresponding to $\phi = 10°$. The critical ϕ for the fastest and the exponential growth depends on ʃ. Therefore, for a given ʃ, the optimal ϕ values exhibit exponential growth in the line element, although this is not the case for all values, as illustrated in Fig. 11(a).

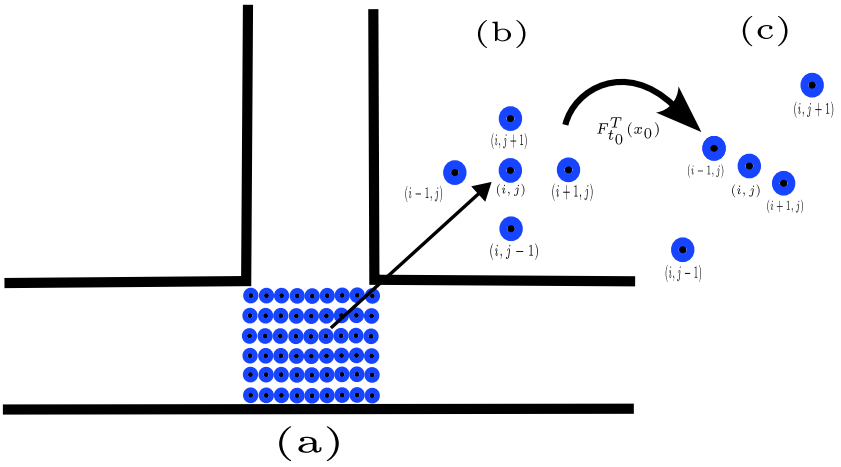

FIG. 12. (a) Initialization of particle locations in the uniform grids at the T-junction, (b) tagged (i, j)th particle and the neighboring particles at $t = t_0$, and (c) location of neighboring particles of tagged (i, j)th particle at $t = T$.

In the second scenario where $\phi = 70^\circ$, the line length increases exponentially for smaller ϱ values, as illustrated in Fig. 11(b), suggesting that reducing ϱ enhances stirring. Similar to the previous scenario, not all ϱ values display exponential growth; only those below a critical value for a given ϕ exhibit this characteristic.

F. Finite-time Lyapunov exponent (FTLE) field

To further illustrate the chaotic behavior resulting from the exponential growth in line length, we identify the most influential material lines where the stretching or shrinking is at its maximum. The FTLE (σ) quantifies this stretch or shrinkage, as described by the following equation [43,44]:

$$\sigma_{t_0}^{T}(\mathbf{x}) = \frac{1}{|T|} \ln \sqrt{\lambda_{\max}(\Gamma)}, \tag{7}$$

where $\Gamma = [\nabla \mathbf{F}_{t_0}^{T}]' \nabla \mathbf{F}_{t_0}^{T}$ is the right Cauchy-Green deformation tensor. Here, $\mathbf{F}_{t_0}^{T}$ denotes the Lagrangian description of fluid motion, known as a flow map, which indicates the final state $(\mathbf{x}, T)$ at a specific time T given an initial state $(\mathbf{x}_0, t_0)$. The symbol ($'$) represents the transpose of the matrix, while $\lambda_{\max}(\Gamma)$ is the maximum eigenvalue of Γ, representing the maximum stretching occurring over the time interval T.

We utilize computer simulations to compute the FTLE, offering a quantitative measure of the rate at which infinitesimally close trajectories diverge, thus revealing regions of significant stretching and stirring in the flow. Initially, we set up a grid of particles at the T-junction with uniform spacing of $\Delta x = 0.1$ and $\Delta y = 0.1$ in the horizontal and vertical directions, respectively, as depicted in Fig. 12(a). Figure 12(b) shows the tagged (i, j)th particle along with its neighboring particles at time $t = t_0$. Inset (c) illustrates the separation of the (i, j)th particle from its neighbors after a time T. This setup enables us to track the motion of each particle within the fluid flow over time.

Next, we determine the trajectory of each particle over a time interval of 10 oscillation cycles using the following differential equation (2). We record the final positions of all particles after 10 oscillation cycles, creating a flow map $\mathbf{F}_{t_0}^{T}$. This map links the initial position of a particle $\mathbf{x}_0$ at time t_0 to its position $\mathbf{x}(T; t_0, \mathbf{x}_0)$ at time T.

We create auxiliary particle grids to compute the gradient of the flow map over the 10 cycles, positioning them at small perturbations $(\delta x, \delta y)$ from the (i, j)th particle [43,45]. These perturbations enable us to approximate the spatial derivatives of the flow map, which are crucial for calculating

the gradient. We express the gradient of the flow map as follows:

$$\nabla F_{t_0}^{t}(\mathbf{x}_0) = \begin{pmatrix} \dfrac{\Delta_{11}}{2|\delta_x|} & \dfrac{\Delta_{12}}{2|\delta_y|} \\ \dfrac{\Delta_{13}}{2|\delta_x|} & \dfrac{\Delta_{22}}{2|\delta_y|} \end{pmatrix}, \tag{8}$$

where $\Delta_{11} = x_1(T;t_0,\mathbf{x}_0+\delta_x) - x_1(T;t_0,\mathbf{x}_0-\delta_x)$, $\Delta_{12} = x_1(T;t_0,\mathbf{x}_0+\delta_y) - x_1(T;t_0,\mathbf{x}_0-\delta_y)$, $\Delta_{21} = x_2(t;t_0,\mathbf{x}_0+\delta_x) - x_2(t;t_0,\mathbf{x}_0-\delta_x)$ and $\Delta_{22} = x_2(t;t_0,\mathbf{x}_0+\delta_y) - x_2(t;t_0,\mathbf{x}_0-\delta_y)$.

Once we have calculated the flow map gradient $\nabla\mathbf{F}_{t_0}^{T}$, we compute the Cauchy-Green strain tensor $C_{t_0}^{T}(\mathbf{x}_0)$, defined as

$$C_{t_0}^{T}(\mathbf{x}_0) = \left[\nabla\mathbf{F}_{t_0}^{T}\right]'\nabla\mathbf{F}_{t_0}. \tag{9}$$

This tensor reveals information about the deformation of fluid elements and identifies the directions and magnitudes of stretching and compression. The eigenvectors of $C_{t_0}^{T}(\mathbf{x}_0)$ align with the most influential stretching and compressing material elements initially located at $\mathbf{x}_0$. Finally, we compute the FTLE field $\sigma_{t_0}^{T}(\mathbf{x}_0)$ using the maximum eigenvalues λ related to the eigenvectors of the Cauchy-Green strain tensor $C_{t_0}^{T}$:

$$\sigma_{t_0}^{T}(\mathbf{x}_0) = \frac{1}{2(T-t_0)}\log\lambda(\mathbf{x}_0). \tag{10}$$

The FTLE field uncovers regions of significant stretching and stirring within the fluid flow, providing valuable insights into the underlying dynamics of the system. This analysis enhances our understanding of the complex interactions within the flow.

G. Extraction of Lagrangian coherent structures

Once we calculate the eigenvalues $\lambda_i(\mathbf{x}_0)$ and eigenvectors $\zeta_i(\mathbf{x}_0)$ associated with $C_{t_0}^{T}(\mathbf{x}_0)$ at $\mathbf{x}_0$, where $i = 1, 2$, we can identify the Lagrangian coherent structures (LCSs), these structures are critical for understanding flow kinematics and material transport within the fluid, we compute tensor lines that are tangent to the eigenvector field $\zeta_1(\mathbf{x})$, which is associated with the maximum eigenvalue $\lambda_1(\mathbf{x})$, these tensor lines represent repelling LCSs, indicating regions where fluid particles diverge over time, thus reflecting zones of maximum stretching. Similarly, the tensor lines tangent to the eigenvector field $\zeta_2(\mathbf{x})$, related to the second eigenvalue $\lambda_2(\mathbf{x})$, represent attracting LCSs. Fluid parcels converge over time in these regions, signifying zones of maximum compression.

We analyze the flow map of fluid trajectories from $t = 0$ to $t = 10\ T$ in our simulations to compute the FTLE field at $t = 0$, initialized over a grid at the T-junction. Figure 13 displays the FTLE fields for both the nonchaotic case ($\mathfrak{f} = 0.5$ and $\phi = 10^\circ$) and the chaotic case ($\mathfrak{f} = 0.5$ and $\phi = 70^\circ$). In the chaotic scenario, the maximum stretch rate is approximately an order of magnitude higher than in the nonchaotic case. We identify sharp ridges in the FTLE fields as potential Lagrangian coherent structures (LCSs), which act as transport barriers in the flow. Utilizing variational theory [46], we extract LCSs associated with chaotic advection by computing tensor lines. The tensor lines that align with the eigenvector field of the maximum eigenvalue of the strain-rate tensor Γ define repelling LCSs. Conversely, those aligned with the minimum eigenvalue represent attracting LCSs. In Fig. 13(b), we highlight the most prominent repelling LCSs with a dotted line and the attracting LCSs with a dashed line, illustrating their roles in driving chaotic flow dynamics.

H. Regime map

We create a regime map on the $\mathfrak{f}$-ϕ parameter plane to identify regions that exhibit different stretch-fold behaviors and to highlight areas where chaos occurs. By combining experimental results with numerical simulations, we confirm the stretching behavior in various regions, distinguishing

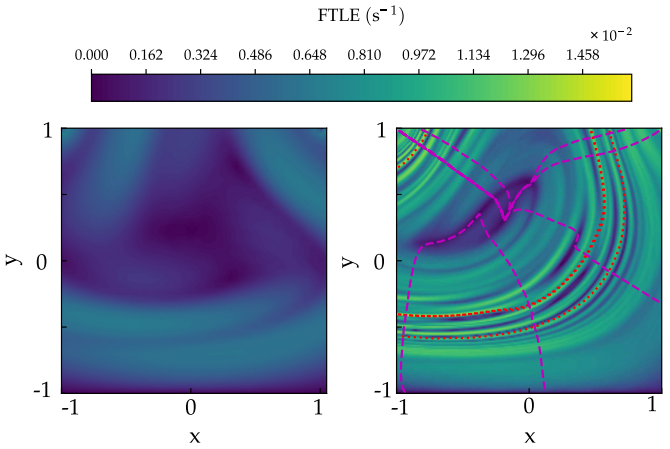

FIG. 13. Finite-time Lyapunov exponent (FTLE) fields showing (left) nonchaotic stirring at $\mathfrak{f} = 0.5$ and $\phi = 10^\circ$ and (right) chaotic stirring at $\mathfrak{f} = 0.5$ and $\phi = 70^\circ$. In the chaotic stirring field (right), the red dotted line represents the repelling Lagrangian coherent structure (LCS), while the magenta dashed line indicates the attracting LCS.

regions of chaotic line element deformations. As shown in Fig. 14, this map illustrates how the subperiodic variable ϕ and the normalized frequency $\mathfrak{f}$ jointly influence fluid behavior.

At the extremes of the ϕ axis ($\phi = 0^\circ$ and $\phi = 180^\circ$), the trajectories display time-periodic behavior, regardless of the $\mathfrak{f}$ values. These cases correspond to synchronized oscillations, indicating no net line deformation. In contrast, nonzero values of ϕ can lead to either nonchaotic or chaotic deformations of the line element, depending on the $\mathfrak{f}$ value. For any nonzero value of ϕ, decreasing

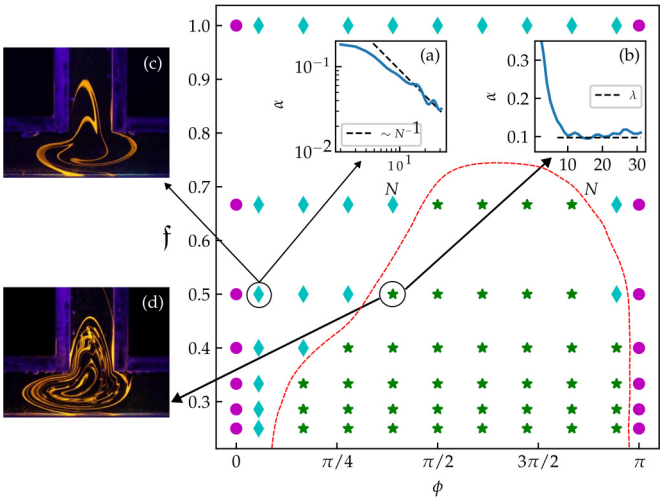

FIG. 14. Regime plot in $\mathfrak{f}$-ϕ parametric plane indicates the regions of nonchaotic and chaotic fluid trajectories. Here, the • symbol represents the time-periodic trajectories, the ♦ symbol represents nonchaotic trajectories, and $*$ indicates chaotic trajectories. The red dashed line is the separating boundary of chaotic and nonchaotic regions. (a) Evolution of α with N for a nonchaotic case ($\phi = 10^\circ$, $\mathfrak{f} = 0.5$), (b) evolution of α with N for a chaotic case ($\phi = 70^\circ$, $\mathfrak{f} = 0.5$), (c) experimental visuals of nonchaotic case ($\phi = 10^\circ$, $\mathfrak{f} = 0.5$) at $N = 10$, and (d) experimental visuals of chaotic case ($\phi = 70^\circ$, $\mathfrak{f} = 0.5$) at $N = 10$.

ƒ can lead the system into chaos. Moreover, at a fixed ƒ, specific optimal values of ϕ are more conducive to chaotic stirring. Additionally, as ƒ decreases, the range of these optimal ϕ values expands.

We selected two representative cases from the regime map shown in Fig. 14: one from the nonchaotic region ($ƒ = 0.5$, $\phi = 10^\circ$) and another from the chaotic region ($ƒ = 0.5$, $\phi = 70^\circ$). For each case, we extracted the parameter α, defined as the ratio of the difference in line length (ΔL) to the difference in cycle number (ΔN), normalized by the current line length. We calculated it using the following formula:

$$\alpha = \frac{1}{L}\left(\frac{\Delta L}{\Delta N}\right).$$

When we consider how α evolves with N, if the line length grows according to a power law, such that $L \sim N^e$, then $\Delta L/\Delta N \sim eN^{e-1}$. We can express this as $(1/L)(\Delta L/\Delta N) \sim eN^{-1}$. Thus, for power-law growth, α scales inversely with N. This scaling behavior appears in the nonchaotic case, as shown in Fig. 14(a). This power-law behavior reflects the limited ability to stretch and fold material lines, resulting in weak stirring. In contrast, when we examine exponential growth in line length, where $L \sim \exp(\lambda t)$, we find that $\Delta L/\Delta N \sim \lambda \exp(\lambda t)$, suggesting that α approaches a constant value, λ, which we observe in the chaotic case, as indicated in Fig. 14(b). The exponential growth of material lines characterizes chaotic stirring, where fluid elements undergo rapid stretching and folding. Additionally, the experimental visuals in Figs. 14(c) and 14(d) correspond to the nonchaotic and chaotic stirring cases, respectively. They demonstrate the distinct stirring features that align with power-law and exponential scaling.

V. CONCLUSION

We conducted experimental and simulation studies to investigate the onset of chaos in a slow, viscous oscillatory flow through a bifurcating geometry. Specifically, we analyze the effects of subperiodic variable oscillations (defined by parameter ϕ) and oscillation frequency (ƒ) on the stretch-fold mechanism of the fluid element leading to chaos. We generated the oscillatory flows using a simple bifurcating network—a T-section equipped with a piston, cylinder, and motor assembly. Our primary goal was to delineate a boundary on the ƒ-ϕ parameter plane that differentiates chaotic from nonchaotic stirring. In the case of symmetric oscillations ($\phi = 0^\circ$ and $\phi = 180^\circ$), the fluid trajectories exhibited time-periodic behavior, leading to zero net deformation and no stirring, irrespective of the ƒ value. Conversely, in subperiodically variable scenarios, disparities in piston velocities result in the coexistence of open and closed streamlines, which resemble the characteristics of "tendrils" and "whorls," leading to the stretching and folding of line elements. Closed streamlines are generated due to the interaction between the flow streams of unequal magnitudes at the T-junction, subsequently creating Moffatt eddies in the arm with the weaker flow.

We delineate the region of chaotic stirring on the ƒ-ϕ parametric plane and highlight how ƒ and ϕ interact to initiate stirring and facilitate the transition to a chaotic state. Our findings show that fluid stirring can occur for $0^\circ < \phi < 180^\circ$ at a given ƒ, but only a select few optimal ϕ values lead to chaos, resulting in efficient stirring. We identify this through the exponential growth of line elements, accompanied by a maximal stretching rate observed in the FTLE field. However, as ƒ decreases, the optimal range of ϕ that induces chaotic stirring expands, suggesting that a combination of optimal ϕ values and lower ƒ levels promotes chaos.

This study utilized a simple bifurcating network to facilitate different flow behaviors by modulating the inlet conditions. These findings have significant practical implications, with potential applications in micromixer design and a deeper understanding of complex fluid dynamics in physiological and biological systems. However, further research is necessary to explore the fluid kinematics with more complex geometries and different time modulation protocols of the inlet boundary conditions, which would more closely approximate practical scenarios.

[1] L. Pratt, I. Rypina, T. Özgökmen, P. Wang, H. Childs, and Y. Bebieva, Chaotic advection in a steady, three-dimensional, Ekman-driven eddy, J. Fluid Mech. **738**, 143 (2014).
[2] I. Rypina, L. Pratt, P. Wang, T. Özgökmen, and I. Mezic, Resonance phenomena in a time-dependent, three-dimensional model of an idealized eddy, Chaos **25**, 087401 (2015).
[3] J. M. Ottino and S. Wiggins, Introduction: Mixing in microfluidics, Philos. Trans. R. Soc. London, Ser. A **362**, 923 (2004).
[4] A. W. Nienow, M. F. Edwards, and N. Harnby, *Mixing in the Process Industries* (Butterworth-Heinemann, Oxford, UK, 1997).
[5] F. Raynal and J.-N. Gence, Energy saving in chaotic laminar mixing, Int. J. Heat Mass Transfer **40**, 3267 (1997).
[6] M. Alvarez-Hernández, T. Shinbrot, J. Zalc, and F. Muzzio, Practical chaotic mixing, Chem. Eng. Sci. **57**, 3749 (2002).
[7] J. B. West, *Respiratory Physiology: The Essentials* (Lippincott Williams & Wilkins, Philadelphia, PA, 2012).
[8] C. Kleinstreuer and Z. Zhang, Airflow and particle transport in the human respiratory system, Annu. Rev. Fluid Mech. **42**, 301 (2010).
[9] J. Sznitman, Respiratory microflows in the pulmonary acinus, J. Biomech. **46**, 284 (2013).
[10] S. Verbanck and M. Paiva, Gas mixing in the airways and airspaces, Compr. Physiol. **1**, 809 (2011).
[11] J. Sznitman, Revisiting airflow and aerosol transport phenomena in the deep lungs with microfluidics, Chem. Rev. **122**, 7182 (2022).
[12] M. Davidson and J. Fitz-Gerald, Flow patterns in models of small airway units of the lung, J. Fluid Mech. **52**, 161 (1972).
[13] F. Cinkotai, Fluid flow in a model alveolar sac, J. Appl. Physiol. **37**, 249 (1974).
[14] J. Ultman, Gas transport in the conducting airways, *Gas Mixing and Distribution in the Lung*, edited by L. A. Engel, and M. Paiva (Dekker, New York, 1985), Chap. 3.
[15] A. Tsuda, F. S. Henry, and J. P. Butler, Chaotic mixing of alveolated duct flow in rhythmically expanding pulmonary acinus, J. Appl. Physiol. **79**, 1055 (1995).
[16] J. Butler and A. Tsuda, Effect of convective stretching and folding on aerosol mixing deep in the lung, assessed by approximate entropy, J. Appl. Physiol. **83**, 800 (1997).
[17] A. Tippe and A. Tsuda, Recirculating flow in an expanding alveolar model: Experimental evidence of flow-induced mixing of aerosols in the pulmonary acinus, J. Aerosol Sci. **31**, 979 (2000).
[18] S. Haber, J. Butler, H. Brenner, I. Emanuel, and A. Tsuda, Shear flow over a self-similar expanding pulmonary alveolus during rhythmical breathing, J. Fluid Mech. **405**, 243 (2000).
[19] A. Tsuda, Y. Otani, and J. P. Butler, Acinar flow irreversibility caused by perturbations in reversible alveolar wall motion, J. Appl. Physiol. **86**, 977 (1999).
[20] H. Kumar, M. H. Tawhai, E. A. Hoffman, and C.-L. Lin, The effects of geometry on airflow in the acinar region of the human lung, J. Biomech. **42**, 1635 (2009).
[21] S. Chhabra and A. K. Prasad, Flow and particle dispersion in a pulmonary alveolus—Part I: Velocity measurements and convective particle transport, J. Biomech. Eng. **132**, 051009 (2010).
[22] D. Ciloglu, A numerical study of the aerosol behavior in intra-acinar region of a human lung, Phys. Fluids **32**, 103305 (2020).
[23] J. M. Ottino, *The Kinematics of Mixing: Stretching, Chaos, and Transport* (Cambridge University Press, Cambridge, UK, 1989).
[24] J. Chaiken, R. Chevray, M. Tabor, and Q. Tan, Experimental study of Lagrangian turbulence in a Stokes flow, Proc. R. Soc. London, Ser. A **408**, 165 (1986).
[25] W.-L. Chien, H. Rising, and J. Ottino, Laminar mixing and chaotic mixing in several cavity flows, J. Fluid Mech. **170**, 355 (1986).
[26] D. Khakhar, H. Rising, and J. Ottino, Analysis of chaotic mixing in two model systems, J. Fluid Mech. **172**, 419 (1986).
[27] J. M. Ottino, The mixing of fluids, Sci. Am. **260**, 56 (1989).
[28] J. M. Ottino *et al.*, Mixing, chaotic advection, and turbulence, Annu. Rev. Fluid Mech. **22**, 207 (1990).

[29] H. Aref, Stirring by chaotic advection, J. Fluid Mech. **143**, 1 (1984).
[30] H. Aref, The development of chaotic advection, Phys. Fluids **14**, 1315 (2002).
[31] H. Aref and S. Balachandar, Chaotic advection in a Stokes flow, Phys. Fluids **29**, 3515 (1986).
[32] W. Hackborn, M. E. Ulucakli, and T. Yuster, A theoretical and experimental study of hyperbolic and degenerate mixing regions in a chaotic Stokes flow, J. Fluid Mech. **346**, 23 (1997).
[33] E. Gouillart, N. Kuncio, O. Dauchot, B. Dubrulle, S. Roux, and J.-L. Thiffeault, Walls inhibit chaotic mixing, Phys. Rev. Lett. **99**, 114501 (2007).
[34] E. Gouillart, J.-L. Thiffeault, and O. Dauchot, Rotation shields chaotic mixing regions from no-slip walls, Phys. Rev. Lett. **104**, 204502 (2010).
[35] J.-L. Thiffeault, E. Gouillart, and O. Dauchot, Moving walls accelerate mixing, Phys. Rev. E **84**, 036313 (2011).
[36] Emmanuel Villermaux, Mixing versus stirring, Annu. Rev. Fluid Mech. **51**, 245 (2019).
[37] See Supplemental Material at http://link.aps.org/supplemental/10.1103/PhysRevFluids.10.064101 for animations illustrating the pistons' motion for varying ϕ values, along with an experimental video showcasing the line length deformation (both continuous and discrete) for a nonchaotic scenario and a chaotic one, and which includes Refs. [47–65].
[38] T. Papanastasiou, G. Georgiou, and A. N. Alexandrou, *Viscous Fluid Flow* (CRC Press, Boca Raton, FL, 2021).
[39] R. J. Cornish, Flow in a pipe of rectangular cross-section, Proc. R. Soc. London, Ser. A. **120**, 691 (1928).
[40] H. K. Moffatt, Viscous and resistive eddies near a sharp corner, J. Fluid Mech. **18**, 1 (1964).
[41] R. F. Weiss and B. H. Florsheim, Flow in a cavity at low Reynolds number, Phys. Fluids **8**, 1631 (1965).
[42] F. Pan and A. Acrivos, Steady flows in rectangular cavities, J. Fluid Mech. **28**, 643 (1967).
[43] S. C. Shadden, F. Lekien, and J. E. Marsden, Definition and properties of Lagrangian coherent structures from finite-time Lyapunov exponents in two-dimensional aperiodic flows, Physica D **212**, 271 (2005).
[44] G. Haller, Lagrangian coherent structures, Annu. Rev. Fluid Mech. **47**, 137 (2015).
[45] G. Haller, *Transport Barriers and Coherent Structures in Flow Data* (Cambridge University Press, Cambridge, UK, 2023).
[46] M. Farazmand and G. Haller, Computing Lagrangian coherent structures from their variational theory, Chaos **22**, 013128 (2012).
[47] M. Liu, F. Muzzio, and R. Peskin, Quantification of mixing in aperiodic chaotic flows, Chaos, Solitons Fractals **4**, 869 (1994).
[48] D. Rothstein, E. Henry, and J. P. Gollub, Persistent patterns in transient chaotic fluid mixing, Nature (London) **401**, 770 (1999).
[49] G. A. Voth, T. Saint, G. Dobler, and J. P. Gollub, Mixing rates and symmetry breaking in two-dimensional chaotic flow, Phys. Fluids **15**, 2560 (2003).
[50] A. Dodge, M.-C. Jullien, Y.-K. Lee, X. Niu, F. Okkels, and P. Tabeling, An example of a chaotic micromixer: The cross-channel micromixer, C. R. Phys. **5**, 557 (2004).
[51] P. Tabeling, M. Chabert, A. Dodge, C. Jullien, and F. Okkels, Chaotic mixing in cross-channel micromixers, Philos. Trans. R. Soc. London, Ser. A **362**, 987 (2004).
[52] F. R. Phelan Jr, N. R. Hughes, and J. A. Pathak, Chaotic mixing in microfluidic devices driven by oscillatory cross flow, Phys. Fluids **20**, 023101 (2008).
[53] C. Leong and J. Ottino, Experiments on mixing due to chaotic advection in a cavity, J. Fluid Mech. **209**, 463 (1989).
[54] A. Tsuda, J. P. Butler, and J. J. Fredberg, Effects of alveolated duct structure on aerosol kinetics. I. Diffusional deposition in the absence of gravity, J. Appl. Physiol. **76**, 2497 (1994).
[55] C. Darquenne and M. Paiva, Two-and three-dimensional simulations of aerosol transport and deposition in alveolar zone of human lung, J. Appl. Physiol. **80**, 1401 (1996).
[56] B. Ma and C. Darquenne, Aerosol deposition characteristics in distal acinar airways under cyclic breathing conditions, J. Appl. Physiol. **110**, 1271 (2011).
[57] B. Ma and C. Darquenne, Aerosol bolus dispersion in acinar airways—Influence of gravity and airway asymmetry, J. Appl. Physiol. **113**, 442 (2012).

[58] J. Sznitman, T. Heimsch, J. H. Wildhaber, A. Tsuda, and T. Rösgen, Respiratory flow phenomena and gravitational deposition in a three-dimensional space-filling model of the pulmonary acinar tree, J. Biomech. Eng. **131**, 031010 (2009).

[59] J. Sznitman, R. Sutter, D. Altorfer, M. Stampanoni, T. Rösgen, and J. C. Schittny, Visualization of respiratory flows from 3D reconstructed alveolar airspaces using x-ray tomographic microscopy, J. Visual. **13**, 337 (2010).

[60] F. Henry, S. Haber, D. Haberthür, N. Filipovic, D. Milasinovic, J. C. Schittny, and A. Tsuda, The simultaneous role of an alveolus as flow mixer and flow feeder for the deposition of inhaled submicron particles, J. Biomech. Eng. **134**, 121001 (2012).

[61] T. Sera, K. Uesugi, N. Yagi, and H. Yokota, Numerical simulation of airflow and microparticle deposition in a synchrotron micro-ct-based pulmonary acinus model, Comput. Methods Biomech. Biomed. Eng. **18**, 1427 (2015).

[62] H. Miki, J. P. Butler, R. A. Rogers, and J. L. Lehr, Geometric hysteresis in pulmonary surface-to-volume ratio during tidal breathing, J. Appl. Physiol. **75**, 1630 (1993).

[63] E. J. Berg, J. L. Weisman, M. J. Oldham, and R. J. Robinson, Flow field analysis in a compliant acinus replica model using particle image velocimetry (piv), J. Biomech. **43**, 1039 (2010).

[64] G. I. Taylor, The formation of emulsions in definable fields of flow, Proc. R. Soc. London A **146**, 501 (1934).

[65] R. N. Valani, B. Harding, and Y. M. Stokes, Active particle motion in Poiseuille flow through rectangular channels, Phys. Rev. E **110**, 034603 (2024).